INTERNATIONAL JOURNAL FOR NUMERICAL METHODS IN FLUIDS, VOL. 16, 859–878 (1993)

NUMERICAL SIMULATION OF VORTEX SHEDDING PAST TRIANGULAR CYLINDERS AT HIGH REYNOLDS NUMBER USING A k–ε TURBULENCE MODEL

STEFAN H. JOHANSSON, LARS DAVIDSON AND ERIK OLSSON

Department of Thermo and Fluid Dynamics, Chalmers University of Technology, S-412 96 Gothenburg, Sweden

SUMMARY

Calculations of unsteady turbulent flow around and behind triangular-shaped flameholders using a finite volume code with a k–ε model of turbulence are presented.

The flow behind the flameholders is found to be unsteady (a von Kármán vortex street appears) with a well defined Strouhal frequency (predicted $Sr = 0{\cdot}27$ compared with an experimental value of 0·25). The predicted profiles of velocity and fluctuating kinetic energy agree well with experiments. The periodic motions in the vortex street are shown to be far more important than the turbulent stochastic motions in exchanging momentum in the transversal direction.

The pressure–velocity coupling is handled with the SIMPLEC pressure correction procedure. The discretization in time is fully implicit and 90 time steps are used to resolve one time cycle. It was found that to capture the vortex street it is very important that the grid spacing is sufficiently fine (180×100).

KEY WORDS Vortex shedding Unsteady Turbulent SIMPLEC LES

1. INTRODUCTION

The design process of combustion chambers for gas turbine engines has until recently relied entirely on experimental testing and evaluation of these tests as well as engineering/engineers' know-how. The reasons for this are that the highly turbulent flow field and the turbulence-controlled chemical reactions taking place have been impossible to resolve numerically owing to limitations in computer capability and numerical models. Since computers grow faster and more powerful every day, it will be possible to use more accurate numerical schemes, turbulence and chemical models in the future. In order to construct a work tool which can be used in the design process of a combustion chamber, the numerical models must be tested and validated against experiments. This is the object of the present research project which is being carried out in co-operation with Volvo Flygmotor AB (VFA). At the Department of Thermo and Fluid Dynamics we are working on numerical simulations and at VFA both numerical simulations[1] and experimental investigations[2] are carried out.

In military aerospace engines there are two different types of combustion chambers: the main combustion chamber and the afterburner. In the first type of combustion chamber the fuel and oxidizer are fed into the combustor from two or more streams. The resulting flame is called a diffusion flame, since the reactants must diffuse to mix and eventually react with one another. In the second type of combustion chamber the fuel and oxidizer are already mixed and the resulting flame is called a premixed flame. To prohibit immediate extinction of a flame in the afterburner,

0271–2091/93/100859–20$15.00

Received March 1992
Revised October 1992

the velocity levels must be reduced in some areas. This is commonly achieved by placing a bluff body in the flow stream. The effect is a wake behind the body where velocities will be sufficiently small. In this wake the mixture can be ignited and the flame will spread throughout the combustion chamber. The flow induced by the bluff body or flameholder will be highly turbulent, unsteady and three-dimensional.

The present work focuses on calculating the unsteady flow behind triangular flameholders. The configurations are two-dimensional and no combustion is included. Two different triangular flameholders have been investigated, one with an afterbody, called a stair, and one without an afterbody. VFA has carried out experimental investigations for these configurations. It was found that a von Kármán vortex street with a well-defined Strouhal number appears behind the flameholders. The Reynolds number is sufficiently high for the flow to be turbulent and thus a turbulence model must be included. A k–ε model has been used in the present work to model the three-dimensional turbulent (random) fluctuations, while the large oscillating structures are resolved using the numerical method. The instantaneous velocity $\tilde{U}_i$ can be written as

$$\tilde{U}_i = \langle U_i \rangle + u_i' = \bar{U}_i + \tilde{u}_i + u_i', \tag{1}$$

where $\langle U_i \rangle$ is the phase-averaged velocity, resolved by the numerical scheme, and u_i' is the stochastic three-dimensional small-scale, i.e. turbulent, motion. $\langle U_i \rangle$ is the sum of the time-mean value $\bar{U}_i$ and the deviation $\tilde{u}_i$ from $\bar{U}_i$.

This concept of resolving the large-scale, organized unsteady motion with the numerical scheme and using a k–ε turbulence model has previously been reported by Claus *et al.*,[3] MacInnes *et al.*,[4] Franke *et al.*,[5] and Kourta and Ha Minh.[6] Claus *et al.* calculated a mixing layer with an imposed motion at a single frequency. Calculations were carried out using an LES method as described above and direct numerical simulation (DNS). No definite conclusion as to which method was the best could be drawn in that work. MacInnes *et al.* used the same concept, LES, as Claus *et al.* and their calculations were carried out at the same configuration as in Reference 3. They reported that the main features of mixing are well captured using this kind of LES modelling and they also established that very fine numerical grids are a necessity in such flows. Franke *et al.* calculated the flow past a rectangular cylinder where a von Kármán vortex street existed according to experiments. They compared three different turbulence models: a k–ε model with wall functions, a two-layer k–ε model and a Reynolds Stress Model (RSM). They found that the first approach did not produce any vortex shedding at all and that the second predicted vortex shedding but with too low a Strouhal number. Only the RSM model produced results in fairly good agreement with experiments. Kourta and Ha Minh calculated the turbulent flow in a backward facing step configuration using a k–ε turbulence model. Their approach was somewhat different from that used in the works above and in the present study. The mean flow in their configuration was not inherently unsteady, although the turbulent fluctuating velocities were of the same order of magnitude as the mean flow. They tried to resolve the large-scale turbulent motion with the numerical scheme. In order to achieve this, they tested different reduced values of the coefficient c_μ used in the k–ε turbulence model. This coefficient relates turbulence parameters to an effective viscosity. In this way they reduced the turbulent length scales modelled by the turbulence model. They found that by reducing c_μ by 25% of its standard value, the predicted reattachment length was computed accurately.

The equations are given in the following section. The finite volume code is briefly described in Section 3, while Section 4 summarizes the boundary conditions. The experimental set-up is presented in Section 5. The results are compared with experiments in Section 6, and conclusions are drawn in the final section.

2. EQUATIONS

2.1. General transport equation

The general transport equation in Cartesian co-ordinates for a variable Φ reads

$$\frac{\partial \rho\langle\Phi\rangle}{\partial\tau}+\frac{\partial}{\partial x_m}(\rho\langle U_m\rangle\langle\Phi\rangle)=\frac{\partial}{\partial x_m}\left(\Gamma_\Phi\frac{\partial\langle\Phi\rangle}{\partial x_m}\right)+\bar{S}^\Phi, \tag{2}$$

where $\bar{S}^\Phi$ denotes the source per unit volume for the variable Φ. Define a flux vector J_m containing convection and diffusion as follows:

$$J_m=\rho\langle U_m\rangle\langle\Phi\rangle-\Gamma_\Phi\frac{\partial\langle\Phi\rangle}{\partial x_m}. \tag{3}$$

Integration over a typical control volume with volume V and surface A using the Gauss law yields

$$\int_V\frac{\partial\rho\langle\Phi\rangle}{\partial\tau}\,\mathrm{d}V+\int_A\mathbf{J}\cdot\mathrm{d}\mathbf{A}=\int_V\bar{S}^\Phi\mathrm{d}V. \tag{4}$$

2.2. Mean flow equations

The continuity equation and the unsteady momentum equation read

$$\frac{\partial}{\partial x_i}(\rho\langle U_i\rangle)=0, \tag{5}$$

$$\frac{\partial}{\partial\tau}(\rho\langle U_i\rangle)+\frac{\partial}{\partial x_j}(\rho\langle U_i\rangle\langle U_j\rangle)=-\frac{\partial\langle p\rangle}{\partial x_i}+\frac{\partial}{\partial x_j}\left(\mu_{\text{eff}}\frac{\partial\langle U_i\rangle}{\partial x_j}\right). \tag{6}$$

2.3. Turbulence model

The standard k–ε turbulence model is used. The unsteady transport equations for k and ε can be written in tensor notation as

$$\frac{\partial}{\partial\tau}(\rho\langle k\rangle)+\frac{\partial}{\partial x_i}(\rho\langle U_i\rangle\langle k\rangle)=\frac{\partial}{\partial x_i}\left[\left(\mu+\frac{\mu_t}{\sigma_k}\right)\frac{\partial\langle k\rangle}{\partial x_i}\right]+P_k-\rho\langle\varepsilon\rangle, \tag{7}$$

$$\frac{\partial}{\partial\tau}(\rho\langle\varepsilon\rangle)+\frac{\partial}{\partial x_i}(\rho\langle U_i\rangle\langle\varepsilon\rangle)=\frac{\partial}{\partial x_i}\left[\left(\mu+\frac{\mu_t}{\sigma_\varepsilon}\right)\frac{\partial\langle\varepsilon\rangle}{\partial x_i}\right]+\frac{\varepsilon}{k}(c_{\varepsilon1}P_k-c_{\varepsilon2}\rho\langle\varepsilon\rangle). \tag{8}$$

Since the flow is considered incompressible, the density in equations (5)–(8) is constant. The generation term P_k has the following form in tensor notation:

$$P_k=\mu_t\frac{\partial\langle U_i\rangle}{\partial x_j}\left(\frac{\partial\langle U_i\rangle}{\partial x_j}+\frac{\partial\langle U_j\rangle}{\partial x_i}\right). \tag{9}$$

The turbulent viscosity μ_t is calculated as

$$\mu_t=\rho c_\mu\frac{\langle k\rangle^2}{\langle\varepsilon\rangle}$$

and the effective viscosity μ_{eff} is obtained as

$$\mu_{\text{eff}} = \mu + \mu_t.$$

3. THE CODE

3.1. Basics

In this section the finite volume computer programme CALC-BFC (boundary-fitted co-ordinates) for three-dimensional complex geometries is presented. The code is described in detail in Reference 7, but its main features are given below for convenience. The programme uses Cartesian velocity components as have been used e.g. by Shyy *et al.*[8] and Braaten and Shyy.[9] In most finite volume programmes staggered grids for the velocities have been used.[10] In the present work collocated variables are used, which means that velocities are stored at the same place as all scalar variables such as p, k, ε. This concept, suggested by Rhie and Chow,[11] has been used e.g. by Burns and Wilkes,[12] Peric *et al.*[13] and Miller and Schmidt.[14]

Equation (4) is discretized using standard control volume formulation as described in Reference 10. The integration of equation (4) over a control volume (see Figure 1) gives

$$(\mathbf{J}\cdot\mathbf{A})_e + (\mathbf{J}\cdot\mathbf{A})_w + (\mathbf{J}\cdot\mathbf{A})_n + (\mathbf{J}\cdot\mathbf{A})_s = S^{\Phi}\delta V.$$

Note that the positive signs on the terms containing contributions from the west and south surfaces will be negative because these scalar products in themselves are negative.

The discretized equation will be of the form

$$a_P\langle\Phi\rangle_P = \sum a_{nb}\langle\Phi\rangle_{nb} + S_C^{\Phi}, \tag{10}$$

where

$$a_P = \sum a_{nb} - S_P^{\Phi}.$$

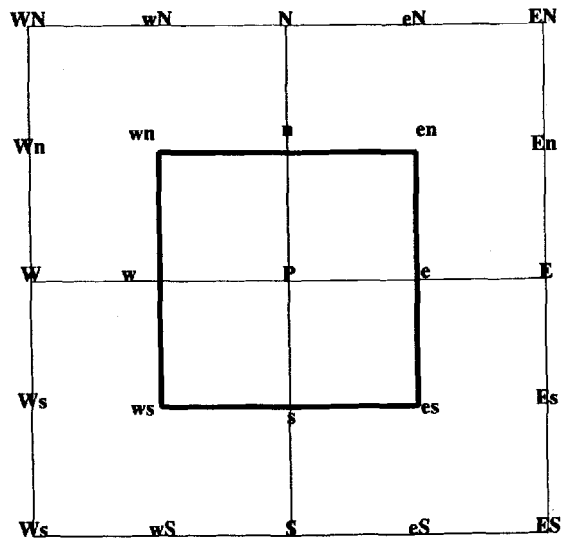

Figure 1. Grid nomenclature. The grid is drawn using Cartesian co-ordinates for clarity. Bold lines construct a typical control volume

The coefficients a_{nb} contain contributions due to both convection and diffusion, while the source terms S_C^Φ and S_P^Φ contain the remaining terms.

3.2. *Time derivatives*

The scheme is fully implicit in time and of first order. It is therefore crucial that sufficiently small time steps are used to minimize the discretization error.

3.3. *Convection*

The convection, which is the first part of the flux vector **J**, is the scalar product of the velocity vector and the area vector multiplied by the density. For an east face this gives

$$\dot{m} = \rho \mathbf{u} \cdot \mathbf{A} = \rho_e (U_e A_{ex} + V_e A_{ey}),$$

and since the Cartesian areas A_{ex} and A_{ey} are stored in the programme, the calculation of the convective contributions to **J** is straightforward. Special care must be taken, however, to avoid non-physical oscillations when the velocities are interpolated from their storage location at the cell centre to the control volume faces. Rhie and Chow[11] solved this problem.

Calculation of the velocities at the control volume faces is described below. For simplicity, Cartesian co-ordinates are used.

When the pressure gradient is added to the momentum equation, standard linear interpolation is used, i.e.

$$\left(\frac{\partial \langle p \rangle}{\partial x}\right)_P = \frac{p_e - p_w}{|\mathbf{we}|},$$

where

$$p_e = f_x \langle p \rangle_E + (1 - f_x) \langle p \rangle_P.$$

When calculating the velocity at the east face, for example, the pressure gradient is subtracted so that

$$U_P^\# = \langle U \rangle_P - \frac{-(p_e - p_w)\delta V}{|\mathbf{we}|(a_P)_P},$$

$$U_E^\# = \langle U \rangle_E - \frac{-(p_{Ee} - p_e)\delta V}{|\mathbf{e(Ee)}|(a_P)_E},$$

where a_P is the discretized coefficient in the U-momentum equations (see equation (10)). The U-velocity at the east face of the control volume is now calculated as

$$U_e = f_x U_E^\# + (1 - f_x) U_P^\# - \frac{(\langle p \rangle_E - \langle p \rangle_P)\delta V}{|\mathbf{PE}|(a_P)_e}.$$

The advantage of this last expression is obvious: now the pressure gradient is calculated using the adjacent nodes of face 'e'. This prevents non-physical oscillations in the pressure field.

The convective terms are discretized using a hybrid upwind/central differencing scheme.[10]

3.4. *Diffusion*

Diffusion is the second part of the flux vector **J** in equation (3) and has the form

$$\mathscr{D} = (\mathbf{J} \cdot \mathbf{A})_{\text{diff}} = -\Gamma_\Phi \mathbf{A} \cdot \nabla \langle \Phi \rangle.$$

For the east face, for instance, it gives in Cartesian co-ordinates (x, y)

$$-(\Gamma_\Phi \mathbf{A}\cdot\nabla\langle\Phi\rangle)_e = -\left[\Gamma_\Phi\left(A_x\frac{\partial\langle\Phi\rangle}{\partial x}+A_y\frac{\partial\langle\Phi\rangle}{\partial y}\right)\right]_e$$

and in curvilinear co-ordinates (ξ, η)

$$-(\mathbf{A}\cdot\nabla\langle\Phi\rangle)_e = -\left(\mathbf{A}\cdot\mathbf{g}_i g^{ij}\frac{\partial\langle\Phi\rangle}{\partial\xi_j}\right)_e = -\left(|\mathbf{A}|\mathbf{n}\cdot\mathbf{g}_i g^{ij}\frac{\partial\langle\Phi\rangle}{\partial\xi_j}\right)_e. \tag{11}$$

The covariant (tangential) base vectors $\mathbf{g}_1$ and $\mathbf{g}_2$ correspond to the grid lines I and J respectively. The metric tensor is involved because the components of the product $\mathbf{A}\cdot\mathbf{g}_i$ and the derivative $\partial\langle\Phi\rangle/\partial\xi_j$ are both covariant and the product of their (contravariant) base vectors is not equal to zero or one (as in Cartesian co-ordinate systems), since they are non-orthogonal to one another.

The normal vector in equation (11) is equal to the cross product of $\mathbf{g}_2$ and $\mathbf{g}_3$ ($\mathbf{g}_3=\mathbf{e}_z=(0, 0, 1)$, since it is a two-dimensional configuration), i.e.

$$\mathbf{n}=\mathbf{g}_2\times\mathbf{g}_3\equiv\mathbf{g}^1,$$

which from $\mathbf{g}_i\mathbf{g}^j=\delta_i^j$ gives

$$\mathbf{n}\cdot\mathbf{g}_2=0.$$

Equation (11) can now be written as

$$-(\mathbf{A}\cdot\nabla\langle\Phi\rangle)_e = -\left(|\mathbf{A}|\mathbf{n}\cdot\mathbf{g}_1 g^{1j}\frac{\partial\langle\Phi\rangle}{\partial\xi_j}\right)_e = -\left[|\mathbf{A}|\mathbf{n}\cdot\mathbf{g}_1\left(g^{11}\frac{\partial\langle\Phi\rangle}{\partial\xi}+g^{12}\frac{\partial\langle\Phi\rangle}{\partial\eta}\right)\right]_e.$$

The diffusive terms are discretized using central differencing, which is of second-order accuracy.[10]

3.5. *Pressure correction equation*

The discretized continuity equation in one dimension takes the form

$$\dot{m}_e-\dot{m}_w=0, \tag{12}$$

where $\dot{m}$ denotes the mass flux, which is calculated as

$$\dot{m}=\rho\mathbf{A}\cdot\mathbf{u}.$$

In SIMPLEC[10] the mass flux is divided into one old value $\dot{m}^*$ and one correction $\dot{m}'$ to the old one, so that

$$\dot{m}=\dot{m}^*+\dot{m}',$$

and the covariant velocity components are related to the pressure gradient as[15]

$$V_i=-\frac{\delta V}{a_P}\frac{\partial\langle p\rangle}{\partial x_i}, \tag{13}$$

where a_P comes from the discretized U_i-equation (see equation (10)). The mass flux correction at the east face can now be obtained as

$$\dot{m}'_e=(\rho\mathbf{A}\cdot\mathbf{u}')_e=\rho_e(A_{ex}u'_e+A_{ey}v'_e)=(\rho\mathbf{A}\cdot\mathbf{g}^j V'_j)_e.$$

Using equation (13) gives

$$\dot{m}'_e = \left[\rho \mathbf{A} \cdot \left(-\frac{\delta V}{a_P}\frac{\partial p'}{\partial x_j}\mathbf{g}^j\right)\right]_e = -\left(\frac{\delta V \rho}{a_P}\mathbf{A}\cdot\nabla p'\right)_e = 0, \tag{14}$$

where p' is the pressure correction. Equations (12) and (14) give

$$\left(\frac{\delta V \rho}{a_P}\mathbf{A}\cdot\nabla p'\right)_w - \left(\frac{\delta V \rho}{a_P}\mathbf{A}\cdot\nabla p'\right)_e + \dot{m}_e^* - \dot{m}_w^* = 0.$$

This equation is a diffusion equation for the pressure correction p'.

4. BOUNDARY CONDITIONS

4.1. Inlet

In the present calculations the inlet profile for the U-velocity was set to a constant value, where U_{inlet} was calculated from the mass flow used in the experiments. V-velocities at the inlet were set to zero. The turbulent quantities were set as

$$k_{\text{in}} = (0{\cdot}05U_{\text{in}})^2, \qquad \varepsilon_{\text{in}} = \frac{0{\cdot}16k_{\text{in}}^{3/2}}{0{\cdot}2l},$$

where $l = 3H$ denotes the channel height.

4.2. Outlet

The U-velocity was calculated from global continuity, while a zero gradient boundary condition was used for the remaining variables. This boundary condition will be correct if the outlet is placed sufficiently far downstream from the flameholder. In the present work the outlet is placed about 20 flameholder heights downstream of the flameholder.

4.3. Walls

Boundary conditions for the walls are set by using the standard wall functions.[16] This approach relates the velocity components as well as $\langle k \rangle$ and $\langle \varepsilon \rangle$ to the friction velocity u^*, which is obtained from the log-law of the wall.

4.4. Blockage

Blockage of cells means that all dependent variables are set to zero inside the blocked domain, except for pressure for which a zero-gradient boundary condition is used. The blocked cells construct the flameholder. Boundary conditions at nodes adjacent to the blocked region are set using wall functions. About 0·5% of the cells are blocked in these calculations, which must be considered a small percentage in view of the complex geometry (see Figure 5).

5. EXPERIMENTAL SET-UP

The experiments on the Validation Rig were performed at Volvo Flygmotor AB (VFA) in Trollhättan, Sweden, during 1990. Measurements were performed using a two-component laser Doppler velocimetry LDV system.[2] The configuration on which the measurements were performed is shown in Figure 2.

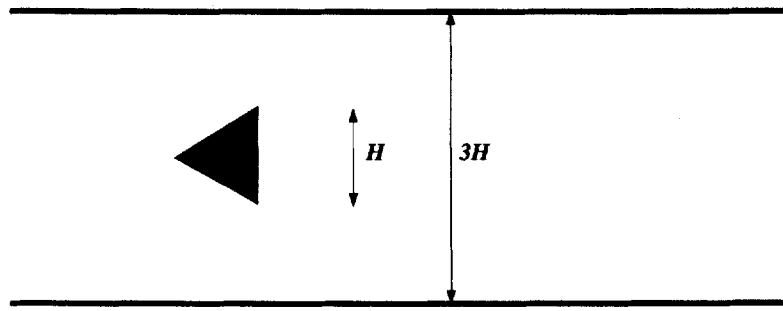

Figure 2. Configuration with flameholder

The Validation Rig is built in modules in order to simplify any modification of the configuration or alteration of the optical access. In order to obtain a uniform flow upstream of the flameholder, some honeycombs and a Mach plate were placed in the upstream flow. This did not produce a perfect two-dimensional uniform flow, but the discrepancies are considered small. Two vortices counter-rotating around the axis parallel to the mean flow direction may be present in the upstream velocity field (A. Sjunnesson, VFA, personal communication, 1991).

Experiments were conducted on two different flameholders: a triangular prism (see Figure 3) and a triangular prism with an afterbody, similar to a stair filling out the wake (see Figure 4). The blockage these flameholders produces is one-third. The total mass flow was $\dot{m}_1 = 0{\cdot}6\ \mathrm{kg\,s^{-1}}$. No combustion comparisons are given in this report, since up to now we have been concentrating on the cold flow.

6. RESULTS

6.1. *Flameholder*

The results from the calculations of the two-dimensional unsteady turbulent flow around and behind a triangular flameholder, with a Reynolds number $U_{in}H/\nu$ of about 45 000, are presented here. Unsteady behaviour is due to vortex shedding, with vortices alternately shedding from the upper and lower edges of the flameholder, forming a von Kármán vortex street behind the flameholder. It may be mentioned that no triggering was used to get unsteady results, but the unsteadiness in the calculated results evolved naturally.

In Figure 5 the grid near the flameholder is shown. The blocked cells which comprise the flameholder are marked with dots. The total grid consists of 180×100 grid points. Some calculations have also been carried out using a 180×200 grid. Velocity profiles obtained with this refined grid were identical to these presented below, which indicates that the results obtained with the 180×100 grid are grid-independent.

To illustrate the periodicity of the flow, the $\langle V \rangle$-velocity taken behind the flameholder is presented as a function of time in Figure 6. It can be seen that an almost perfect periodicity exists, with a well-defined frequency. A cycle time of about 9 ms, using 90 time steps of $\Delta\tau = 0{\cdot}1$ ms in the calculations, gives a Strouhal number

$$Sr = \frac{fH}{\bar{U}_{\mathrm{inlet}}} \tag{15}$$

of 0·27, which should be compared with the experimental value of 0·25. To further illustrate the periodicity of the flow, pressure contours for four different times in a typical cycle are shown in

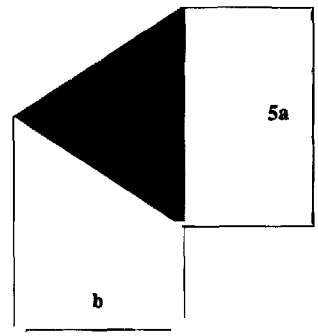

Figure 3. Flameholder: $a = 8$ mm, $b = 34{\cdot}6$ mm

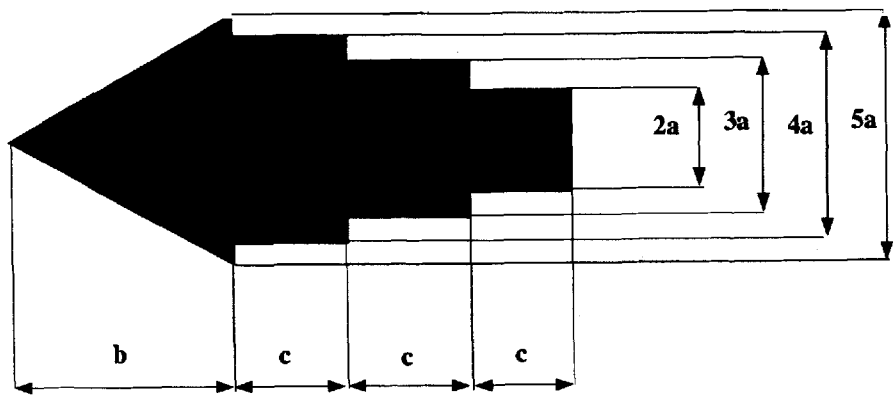

Figure 4. Flameholder with stair: $a = 8$ mm, $b = 34.6$ mm, $c = 17$ mm

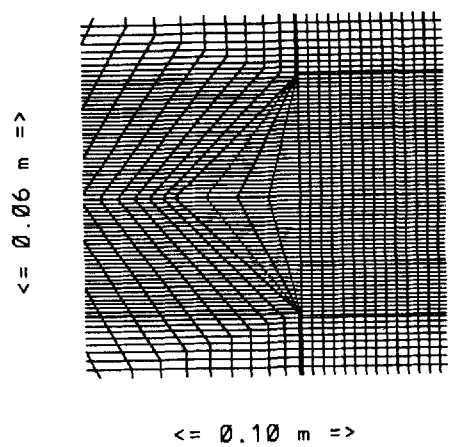

Figure 5. Grid near flameholder

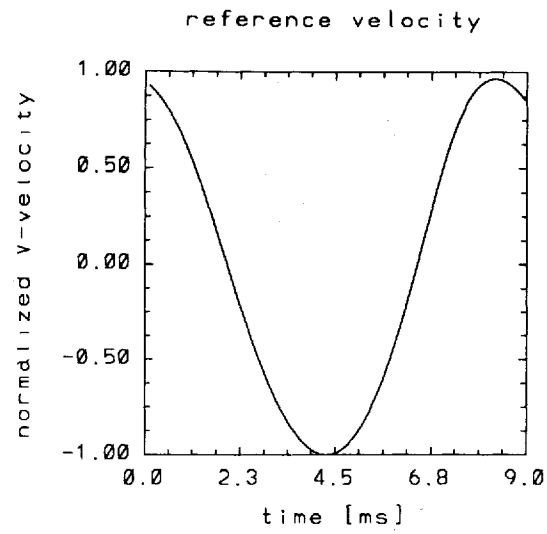

Figure 6. Normalized $\langle V \rangle$-velocity

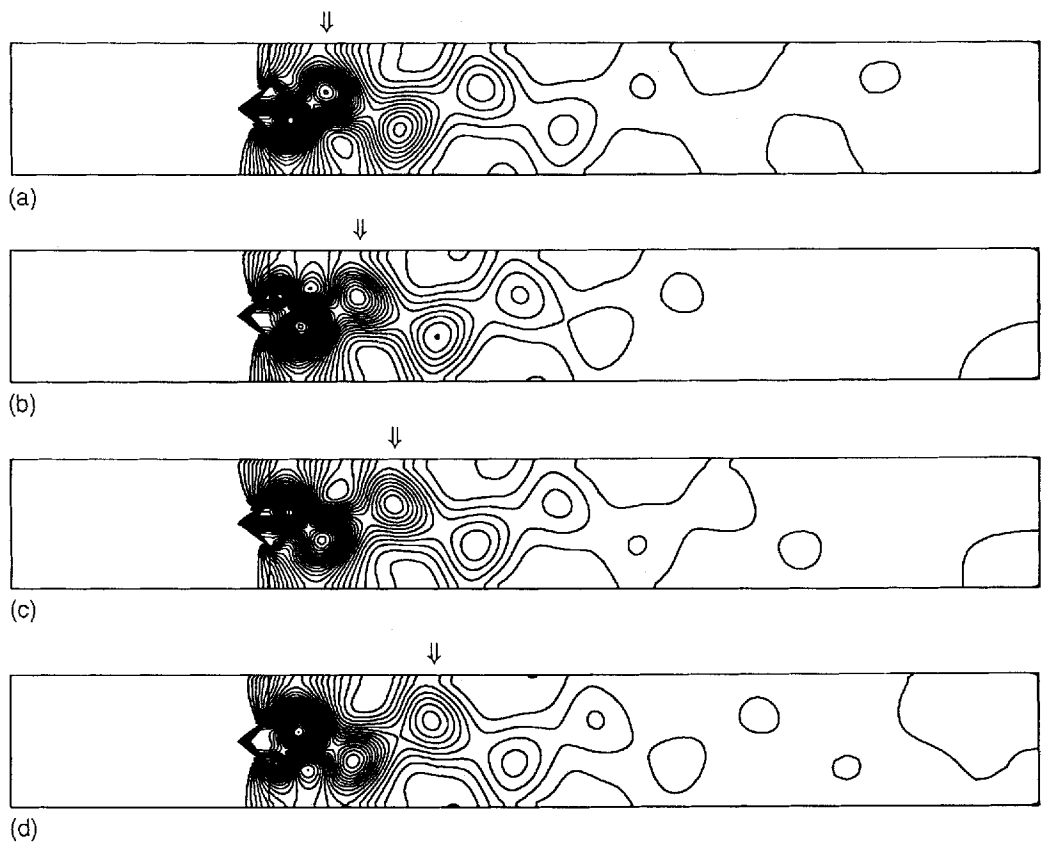

Figure 7. Predicted pressure contours at different times: (a) $\tau = 2{\cdot}2$ ms, (b) $\tau = 4{\cdot}4$ ms, (c) $\tau = 6{\cdot}6$ ms, (d) $\tau = 8{\cdot}8$ ms. The arrow above each figure indicates the position of a chosen vortex as it is convected downstream. The cycle time is approximately 9 ms

Figure 7. From Figure 7(a) to Figure 7(d) almost one cycle has been completed. It is interesting to follow one vortex and see how it is convected downstream as time increases. A vortex also loses strength while being convected downstream, because the turbulent fluctuation field, through the production term (see equation (9)), is continuously extracting energy from the mean flow field. The increased distances between isobars downstream show us that the vortex is constantly losing vorticity, and sufficiently far downstream it will cease to exist. It is, for example, possible to study a vortex that has just been formed close to the upper corner of the flameholder and follow it in time through Figure 7(a)–7(d). In Figure 7(d) a new vortex is being formed at the same location where the previous one was formed. Figure 8 shows a velocity vector plot for the near-flameholder region. A vortex has just been formed at the upper edge of the flameholder and has begun to be convected downstream (cf. Figure 7(a)). At the lower edge a new vortex is beginning to form. Figure 8 shows clearly the non-symmetrical behaviour of the instantaneous flow field, while the time-averaged mean fields will always be symmetric or antisymmetric.

Experimental data for $\bar{U}$, $\bar{V}$, U_{rms} and V_{rms} at five different locations behind the flameholder as well as at the centreline are available. In Figure 9 the $\bar{U}$-velocity at the centreline is presented. Predictions compare well with experiments. The length of the mean recirculation region is computed accurately but the location of maximum negative $\bar{U}$-velocity is predicted slightly upstream as compared with experiments. In some previous attempts with this configuration, steady calculations were carried out using symmetry boundary conditions at the centreline. This resulted in a predicted recirculation region three times longer than in experiments. The unsteady mean flow increases the exchange of momentum between the wake and its surroundings (see further discussion below), which explains why the recirculation zone is reduced in unsteady calculations and hence the necessity of unsteady calculations.

The calculated $\bar{U}$-velocity 15 mm behind the flameholder (Figure (10a)), is in reasonably good agreement with experiments, except close to the symmetry line where the $\bar{U}$-velocity is underpredicted. The flow close to the flameholder is very complex and changes rapidly (see Figure 8). For the locations of 38, 61 and 150 mm behind the flameholder (Figures 10(b)–(d)), the calculations compare very well with experimental results. At the last location, 376 mm behind the flameholder (Figure 10(e)), experiments show nothing that resembles wake flow, whereas the calculations do show some memory of it.

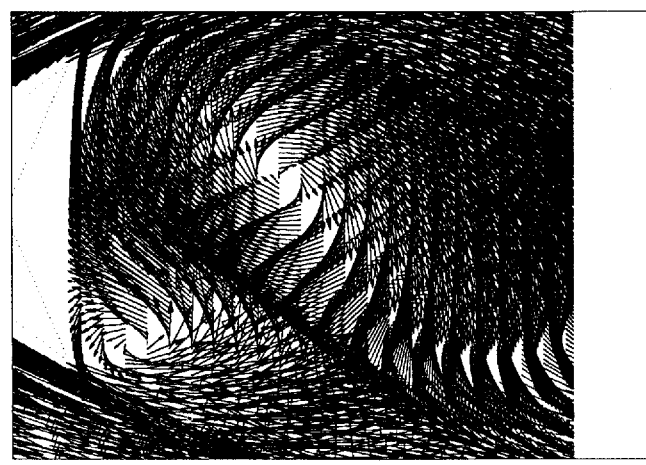

Figure 8. Instantaneous velocity field. In the centre is a vortex that has rolled up at the upper edge and a new vortex is beginning to roll up at the lower edge

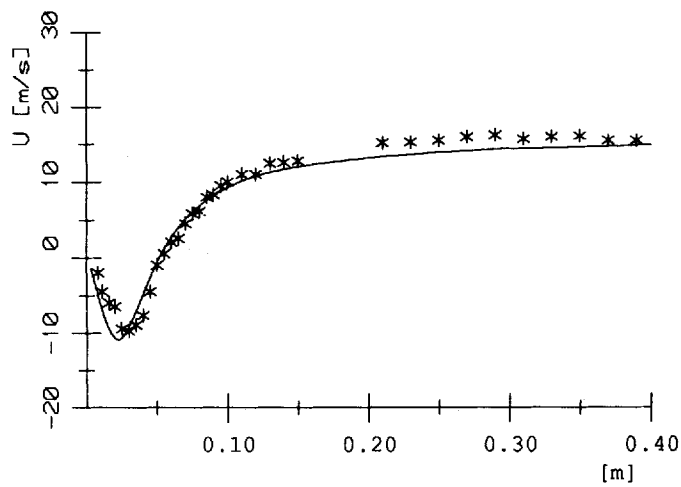

Figure 9. $\bar{U}$-velocity at centreline: ——, calculations: *, experiments

To be able to compare the calculated fluctuating kinetic energy with the fluctuating kinetic energy in the experiments, where the RMS values of U and V are measured, we compare

$$K_{\text{exp, tot}} = \tfrac{1}{2}(U^2_{\text{rms, exp}} + V^2_{\text{rms, exp}}) \tag{16}$$

with

$$K_{\text{calc, tot}} = \tfrac{1}{2}(U^2_{\text{rms, calc}} + V^2_{\text{rms, calc}}) + \bar{k}, \tag{17}$$

where

$$U_{\text{rms, calc}} = \sqrt{\left(\frac{1}{n}\sum_{l=1}^{n}(\langle U_l\rangle - \bar{U})^2\right)},$$

$$V^2_{\text{rms, calc}} = \sqrt{\left(\frac{1}{n}\sum_{l=1}^{n}(\langle V_l\rangle - \bar{V})^2\right)},$$

i.e. when calculating $K_{\text{calc, tot}}$, the turbulent kinetic energy is superimposed to half of the sum of the variances for the two velocities U and V. In doing this, we assume that $\tilde{w}$ is small in comparison with $\tilde{u}$ and $\tilde{v}$, which is reasonable.

For the location 15 mm behind the flameholder the agreement between experiments and present calculations is very good (see Figure 11(a)). At this location pure turbulent kinetic energy contributes approximately 50% of the total fluctuating kinetic energy. Further downstream the turbulent contribution to the total fluctuating kinetic energy decreases and at 38 and 68 mm the maximum fluctuations are larger in the experiments than in the calculations. This indicates that the vortex shedding is slightly stronger in the experimental flow, which would give a larger transversal exchange of momentum and a faster decay of the velocity defect. This was observed from the velocity profiles (Figure 10), where it can be seen that the wake in the experiments disappears slightly faster than in the calculations. At 150 mm behind the flameholder the calculations again compare well with experiments. The last location situated 376 mm behind the flameholder (Figure 11(e)), shows very low values of fluctuating kinetic energy in both experiments and calculations.

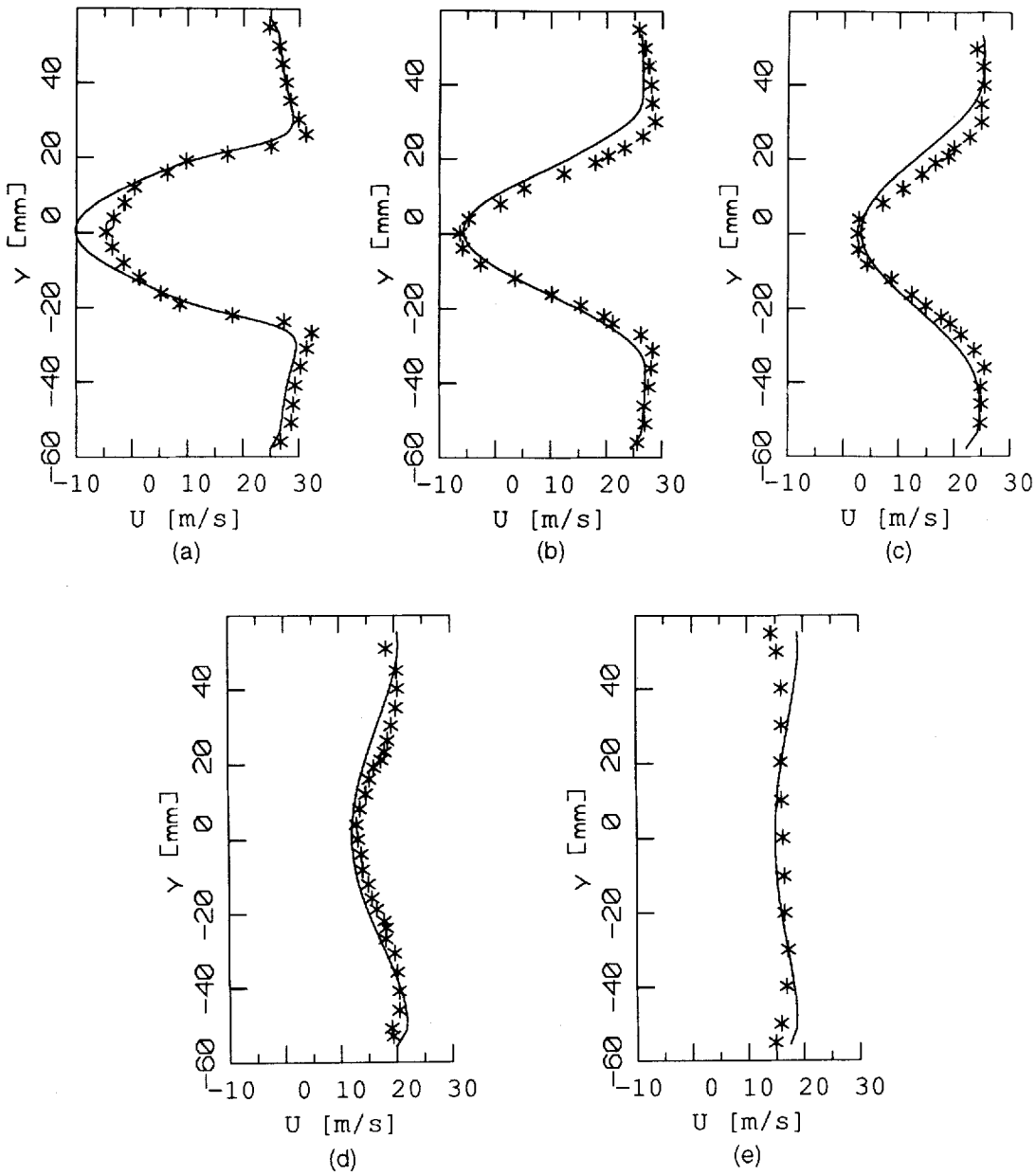

Figure 10. $\bar{U}$-velocities behind the flameholder: ——, calculations; *, experiments; (a) 15 mm, (b) 38 mm, (c) 61 mm, (d) 150 mm, (e) 376 mm

It is interesting to study whether the transport of mean momentum is most affected by turbulent motion, i.e. the Reynolds stresses $\langle u_i' u_j' \rangle$, or by the correlations of velocity fluctuations $\overline{\tilde{u}_i \tilde{u}_j}$ due to the quasi-stationary flow field. Their appearance in the momentum equations is shown

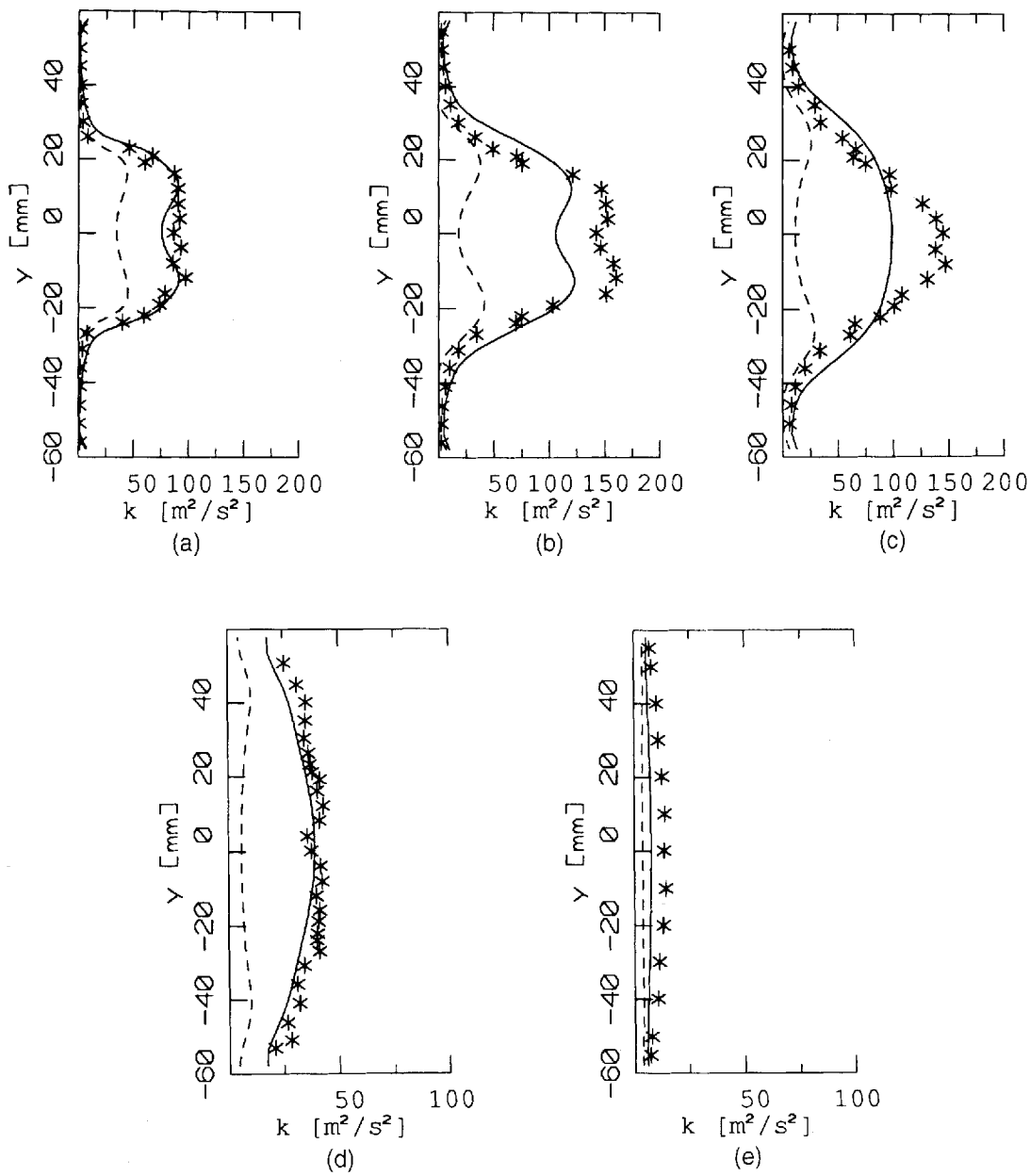

Figure 11. Fluctuating kinetic energies behind the flameholder (see equations (16) and (17): - - -, $\bar{k}$; ——, $K_{\text{calc,tot}}$; *, $K_{\text{exp,tot}}$; (a) 15 mm, (b) 38 mm, (c) 61 mm, (d) 150 mm, (e) 376 mm

below. The instantaneous Navier–Stokes equation reads

$$\frac{\partial \tilde{U}_i}{\partial \tau} + \tilde{U}_j \tilde{U}_{i,j} = -\frac{1}{\rho} \tilde{P}_{,i} + \nu \tilde{U}_{i,jj}. \tag{18}$$

Using Reynolds decomposition (see equation (1)), rearranging equation (18) using the continuity

equation and doing a phase-averaging yields

$$\frac{\partial\langle U_i\rangle}{\partial\tau}+(\langle U_j\rangle\langle U_i\rangle)_{,j}=-\frac{1}{\rho}\langle P_{,i}\rangle+(\nu\langle U_{i,j}\rangle-\langle u_i'u_j'\rangle)_{,j}.$$

This is in principle the general transport equation (see equation (2)) for a velocity component $\langle U_i\rangle$. If a second time averaging is performed, this time over an infinitely long time, the following

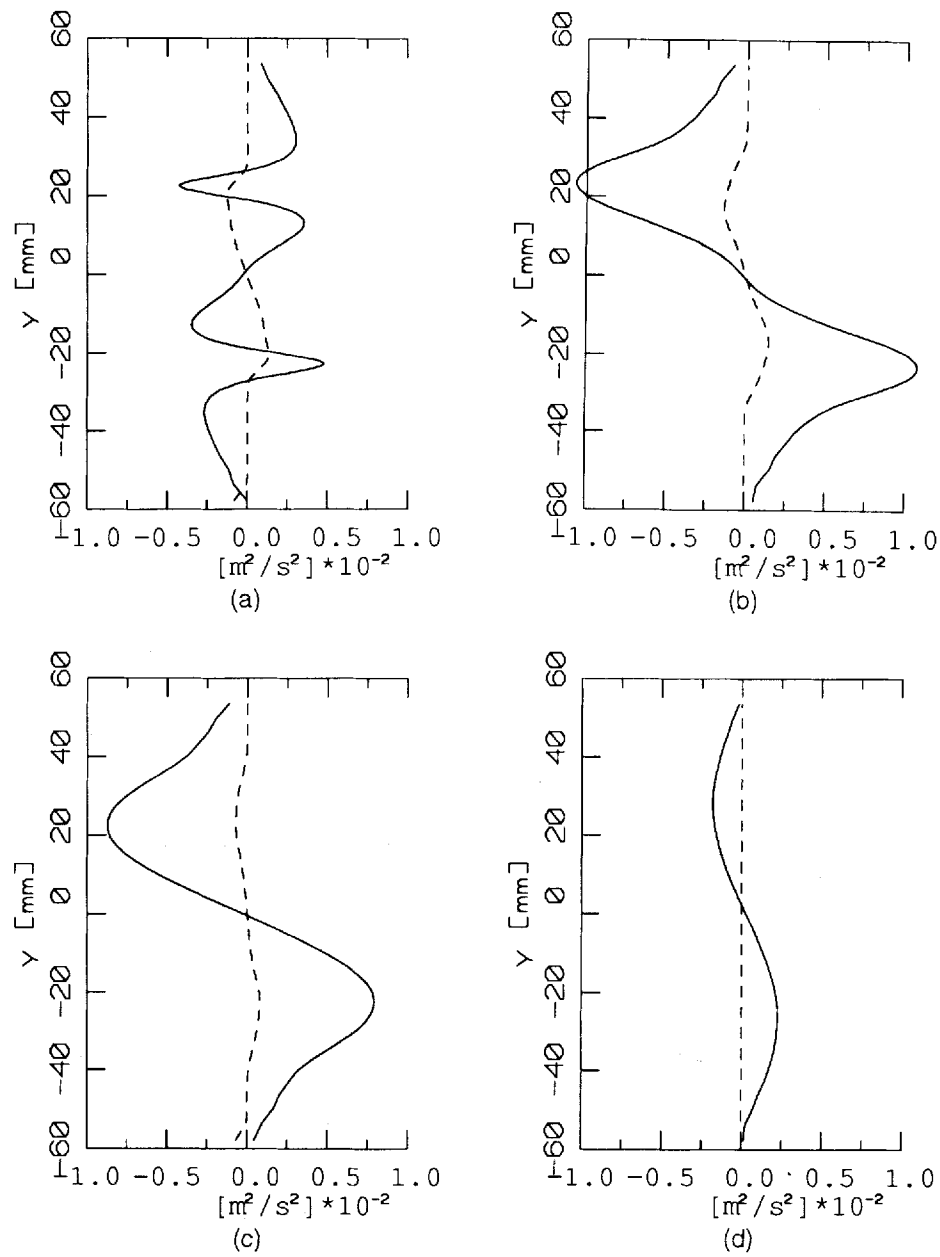

Figure 12. Predicted shear stresses due to periodic and turbulent motions: ——, $\tilde{u}\tilde{v}$; – – –, $\overline{u'v'}$

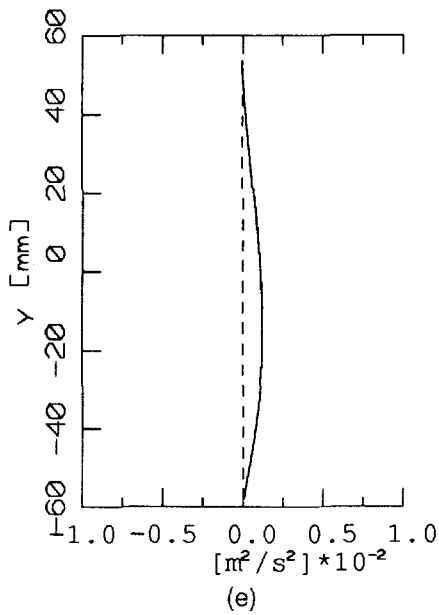

Figure 12. (Continued)

equation is obtained:

$$(\bar{U}_j\bar{U}_i)_{,j} = -\frac{1}{\rho}\bar{P}_{,i} + (\nu\bar{U}_{i,j} - \overline{u_i'u_j'})_{,j} - \overline{(\tilde{u}_i\tilde{u}_j)}_{,j}.$$

When a comparison of the last two terms is performed, one can clearly see that the last one dominates in the whole wake region (see Figure 12), which means that the transversal exchange of momentum is mainly due to periodic motions rather than to turbulent motion.

It can be seen that the profile for the periodic motions has three minima and maxima in Figure 12(a). These seem to be connected with the six inflection points in the velocity profile in Figure 10(a), which is logical: the exchange of momentum is *on average* transported down the velocity gradient. Further downstream the local maxima in the velocity profile in the shear layers have disappeared and the velocity profiles contain only two (interior) inflection points, which correspondingly reduces the number of maxima/minima in the profile of transversal exchange of momentum to two.

6.2. Flameholder with stair

Here the geometrical configuration is somewhat different. An afterbody with the shape of a stair is placed right behind the triangle (see Figure 4). In Figure 13 the $\langle V \rangle$-velocity at a point below the flameholder is presented as a function of time. As in the previous case, a well-defined vortex-shedding frequency exists. The Strouhal number Sr (see equation (15)) is 0·26 here, which should be compared with a value of 0·19 from experiments. The Strouhal number calculated here is approximately the same as in the previous case. In the present calculations the afterbody does not affect the shedding frequency at all, whereas according to experiments it should.

In Figure 14 the $\bar{U}$-velocity at the centreline is presented. In the wake region there is a big difference between present calculations and experiments, because the intensity of the vortices in

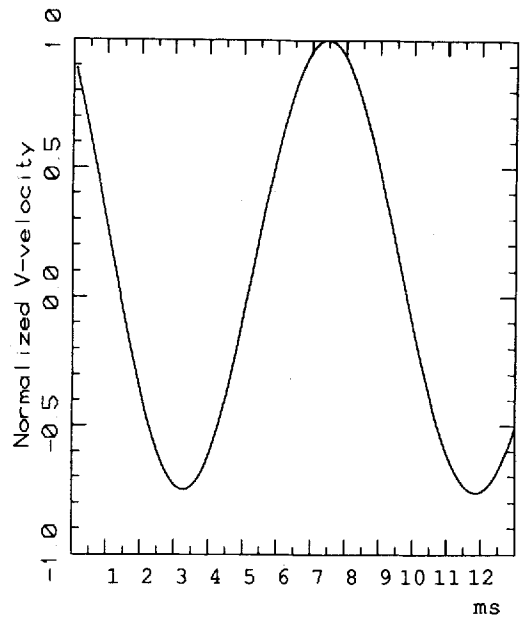

Figure 13. Flameholder with stair. Normalized $\langle V \rangle$-velocity

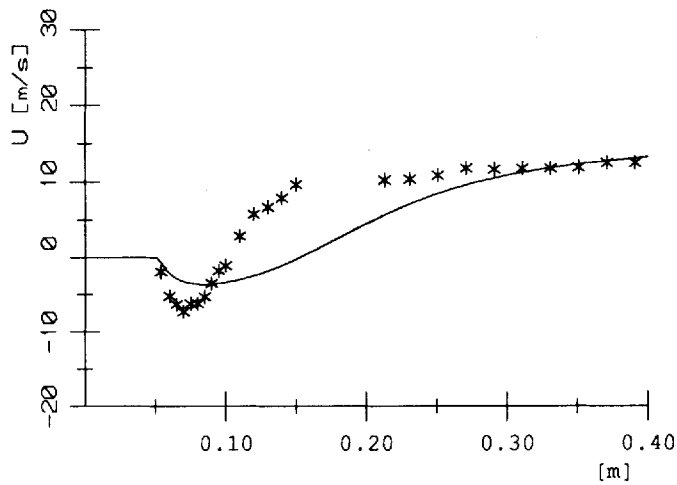

Figure 14. Flameholder with stair. $\bar{U}$-velocity at centreline: ——, calculations; *, experiments

the vortex-shedding motion is underpredicted. This is probably due to the $k-\varepsilon$ turbulence model smoothing out the velocity gradients, which results in too small and too weak vortices in the vortex-shedding motion. In Reference 17 calculations on a quadratic cylinder were carried out and it was concluded that the k–ε turbulence model cannot predict the vortex shedding accurately for such geometries. In the afterbody region, especially where the vortices roll up, the geometry of this case is similar to a quadratic cylinder.

The results are presented in greater detail in Reference 18.

7. CONCLUSIONS

Flow past bluff bodies is often unsteady and at high Reynolds numbers ($Re = 45\,000$ in the present study) it is also turbulent. The instantaneous flow situation is highly complex, with a number of vortices present in the flow. This kind of flow is known as vortex-shedding flow.

In this work the calculations were carried out using a finite volume formulation with collocated variables for the discretization. Velocity–pressure coupling is handled by the SIMPLEC procedure. For closure of the equation system, a standard k–ε turbulence model is used.

The following conclusions can be drawn.

1. Fine numerical grids in space and small time steps are necessary in order to achieve good agreement with experiments.
2. Calculated velocity and fluctuating kinetic energy profiles downstream of the flameholder are in good agreement with experiments.
3. The non-dimensionalized frequency of the vortex-shedding motion, i.e. the Strouhal number Sr, is in good agreement with experiments for the triangular cylinder. The computed Sr is 8% greater than the experimental value.
4. It is concluded that the transport of mean momentum is more affected by the vortex shedding, than by turbulence.
5. A standard k–ε turbulence model can be used to calculate the turbulent influence on unsteady flow fields when the flow is inherently unsteady.
6. When a stair-formed afterbody was added to the triangular cylinder (which resulted in a square-like body), the vortex shedding was strongly underpredicted; this is in line with the results of Franke and Rodi,[17] who found that the k–ε model is not able to predict vortex shedding after square cylinders.

ACKNOWLEDGEMENTS

The financial support of the Swedish Board of Technical Development (STU) and the Swedish Board of Energy Administration (STEV) is gratefully acknowledged.

APPENDIX: NOMENCLATURE

a	coefficient in discretized equation
A	area
c_μ, $c_{\varepsilon 1}$, $c_{\varepsilon 2}$	coefficients in turbulence model
f	frequency
g	determinant of g_{ij}
g_{ij}, g^{ij}	covariant and contravariant components of metric tensor
$\mathbf{g}_i$	unit base vector tangential to grid lines
H	height of flameholder
k	turbulent kinetic energy, $\frac{1}{2}\langle u_i' u_i' \rangle$
n	number of time steps in one cycle
$\mathbf{n}$	normal vector
p	pressure
p'	pressure correction
P_k	production term in turbulence model
S^Φ	source term
Sr	Strouhal number

T	cycle time
$\langle u'v' \rangle$	turbulent shear stress
u_i'	turbulent velocity fluctuation
$\tilde{u}_i$	$\langle U_i \rangle - \bar{U}_i$
U, V	Cartesian velocity components
U_i'	velocity correction
$\tilde{U}_i$	instantaneous velocity in x_i-direction
V_i	covariant velocity component
x, y	Cartesian co-ordinates

Greek letters

Γ	exchange coefficient
δV	volume of control volume
ε	turbulent dissipation rate
μ	dynamic viscosity
ξ, η	co-ordinates along grid lines
ξ_i	co-ordinates along grid lines, tensor notation
ρ	density
$\langle \Phi \rangle$	phase-averaged dependent variable, $(1/N)\Sigma_{m=1}^{N} \Phi(\tau + mT)$
$\bar{\Phi}$	time average of $\langle \Phi \rangle$

Subscripts

calc	calculated
e, w, n, s	referring to control volume faces
E, W, N, S, P	referring to grid nodes
eff	effective
exp	from experiments
rms	root mean square
t	turbulent
Φ	general dependent variable

REFERENCES

1. H. Mårtensson, L. E. Eriksson and P. J. Albråten, 'Numerical simulations of unsteady wakeflow', *Proc. 7th Int. Conf. on Numerical Methods in Laminar and Turbulent Flow*, Pineridge Press, Stanford, Vol. 7, Part 1, 1991, pp. 326–336.
2. A. Sjunnesson, C. Nelson and E. Max, 'LDA measurements of velocities and turbulence in a bluff body stabilized flame', Volvo Flygmotor AB, Trollhättan, 1991.
3. R. W. Claus, P. G. Huang and J. M. Macinnes, 'Time-accurate simulations of a shear layer forced at a single frequency', *AIAA J.*, **28**, 267–275 (1990).
4. J. M. Macinnes, R. W. Claus and P. G. Huang, 'Time dependent calculation of a forced mixing layer using a k–ε turbulence model', *Proc. 7th Symp. on Turbulent Shear Flows*, Stanford, 1989, pp. 11.4.1–11.4.6.
5. R. Franke, W. Rodi and B. Schönung, 'Analysis of experimental vortex-shedding data with respect to turbulence modelling', *Proc. 7th Symp. on Turbulent Shear Flows*, Stanford, 1989, pp. 24.4.1–24.4.6.
6. A. Kourta and H. Ha Minh, 'Modified turbulence model to predict unsteady separated flow', *Proc. 7th Int. Conf. on Numerical Methods in Laminar and Turbulent Flow*, Pineridge Press, Stanford, Vol. 7, Part 1, 1991, pp. 469–479.
7. L. Davidson, 'CALC-BFC: a finite-volume code for complex three-dimensional geometries using collocated variables and Cartesian velocity components', *Rep. 89/10*, Department of Applied Thermodynamics and Fluid Mechanics, Chalmers University of Technology, Gothenburg, 1989.
8. W. Shyy, S. S. Tong and S. M. Correa, 'Numerical recirculating flow calculation using body-fitted coordinate system', *Numer. Heat Transfer*, **8**, 99–113 (1985).
9. M. Braaten and W. Shyy, 'A study of recirculating flow computation using body-fitted coordinates: consistency aspects and mesh skewness', *Numer. Heat Transfer*, **9**, 559–574 (1986).
10. S. V. Patankar, *Numerical Heat Transfer and Fluid Flow*, McGraw-Hill, Washington, DC, 1980.

11. C. M. Rhie and W. L. Chow, 'Numerical study of the turbulent flow past an airfoil with trailing edge separation', *AIAA J.*, **21**, 1527–1532 (1984).
12. A. D. Burns and N. S. Wilkes, 'A finite difference method for the computation of fluid flows in complex three-dimensional geometries', *AERE R 12342*, Harwell Laboratory, 1987.
13. M. Peric, R. Kessler and G. Scheurer, 'Comparison of finite-volume numerical methods with staggered and collocated grids', *Comput. Fluids*, **16**, 389–403 (1988).
14. T. F. Miller and F. W. Schmidt, 'Use of a pressure weighted interpolation method for the solution of the incompressible Navier–Stokes equations on a non-staggered grid system', *Numer. Heat Transfer*, **14**, 213–233 (1988).
15. L. Davidson and P. Hedberg, 'Mathematical derivation of a finite-volume formulation for laminar flow in complex geometries', *Int. j. numer. methods fluids*, **9**, 531–540 (1989).
16. W. Rodi, *Turbulence Models and Their Applications in Hydraulics*, International Association of Hydraulics Research, Delft, 1980.
17. R. Franke and W. Rodi, 'Calculation of vortex shedding past a square cylinder with various turbulence models, *Proc. 8th Symp. on Turbulent Shear Flows*, Munich, 1991, pp. 20.1.1–20.1.6.
18. S. Johansson, 'Numerical simulation of vortex shedding past triangular cylinders', *Publ. 91/7, Thesis Lic. Eng.*, Department of Thermo and Fluid Dynamics, Chalmers University of Technology, Gothenburg, 1991.